Impact of Oxygen Non#Stoichiometry on Near# Ambient Temperature Ionic Mobility in Polaronic Mixed#Ionic#Electronic Conducting Thin Films

Impact of Oxygen Non-Stoichiometry on Near-Ambient Temperature Ionic Mobility in Polaronic Mixed-Ionic-Electronic Conducting Thin Films

Thomas Defferriere[1*], Dmitri Kalaev[1], Jennifer L.M Rupp[1,2], Harry L. Tuller[1]

[1] Department of Material Science and Engineering, Massachusetts Institute of Technology, 77

[2] Department of Electrical Engineering and Computer Science, Massachusetts Institute of Technology, 77 Massachusetts Av., MA, 02139, USA

*tdefferr@mit.edu

Abstract

Enhanced ionic mobility in mixed ionic and electronic conducting solids contributes to improved performance of memristive memory, energy storage and conversion, and catalytic devices. Ionic mobility can be significantly depressed at reduced temperatures, for example, due to defect association and therefore needs to be monitored. Measurements of ionic transport in mixed conductors, however, proves to be difficult due to dominant electronic conductivity. This study examines the impact of different levels of quenched-in oxygen deficiency on the oxygen vacancy mobility near room temperature as measured by a novel dynamic current-voltage analysis. A $Pr_{0.1}Ce_{0.9}O_{2-\delta}$ film was grown by pulsed laser deposition and subsequently annealed, from 400-600° C, in various oxygen partial pressures to modify its oxygen vacancy concentration while minimizing microstructural growth and cation segregation. To

This is the author manuscript accepted for publication and has undergone full peer review but has not been through the copyediting, typesetting, pagination and proofreading process, which may lead to differences between this version and the Version of Record. Please cite this article as doi: 10.1002/adfm.202005640.

monitor changes in film non-stoichiometry, we leverage the existence of an optical absorption center, related to the oxidation state of Pr ions in $Pr_{0.1}Ce_{0.9}O_{2-\delta}$. The oxygen vacancy migration enthalpy was found to exhibit a small increase from 0.73± 0.04 to 0.79 ± 0.02 eV with increasing oxygen deficiency, while the pre-factor was found to increase by a factor of 135. A nearly 13-fold increase in ionic mobility at 60 °C for increases in oxygen non-stoichiometry from 0.032 ± 0.001 to 0.042± 0.001 was thereby detected. Raman spectroscopy was employed to rule out changes in strain as the primary cause for the significant change in mobility. Several factors potentially contributing to the large pre-factor changes are examined and discussed. Insights into how ionic defect concentration can markedly impact ionic mobility should help in elucidating the origins of variations seen in nanoionic devices.

Keywords-Mixed ionic and electronic conductors, small polaron, ionic mobility, nanoionic devices

Introduction

Mixed ionic and electronic conducting (MIEC) oxides are an essential material class for a variety of nanoelectronic, energy, and catalyst applications. These materials simultaneously conduct both electronic and ionic species, enabling them to be used as electrodes for solid oxide fuel cells,[1–3] batteries,[4–12] permeation membranes,[13] active elements in solar to fuel conversion systems,[14–16] and gas sensors[17–19]. At near ambient temperatures, many of these materials become nearly insulating, and here applications instead take advantage of their high-K characteristics (for example, as gate

dielectrics in MOSFET devices or capacitors).[20] However, it is well known that these oxides can suffer from electro-degradation, associated with a long-term decrease of the insulating state of the material under d.c. voltage stress and high temperatures, below the onset of dielectric breakdown. This phenomenon, studied in single crystal materials, was shown to originate from the mobile ionic defects present in the lattice[21,22]. While this mechanism was regarded as an aging effect, determining the lifetime of capacitors or gate dielectrics, progress in nanometric processing methods has enabled the design of novel devices that take advantage of the mobile ionic species, with versatile functionalities that cannot be achieved solely by electronic effects. New memory devices based on ionic defect motion have emerged, for example, in the fields of electronics (e.g. memristors)[12,23–29], magnetics (e.g. magnetoionics)[30–32], optics (e.g. electrochromic devices)[33–36] and ferroelectrics,[37–39] often matching the performance of their electronic counterparts, at lower energy consumption and smaller device footprint. Moreover, these new devices are considered as promising candidates for progressing beyond traditional computational architectures. They do this by enabling analog behavior with time-dependent plasticity phenomena that depend on the diffusive/drift nature of the ionic carriers that can only be emulated by purely electronic counterparts at high energy expenditure.[40–42] This opens up exciting opportunities, for example, in artificial intelligence hardware and neuromorphic computing, allowing for hardware component designs that can mimic basic synaptic functionalities.[29] Nevertheless, due to the much lower mobilities associated with ionic rather than electronic carriers, such MIEC materials tend to be predominately electronically conductive in their behavior at near ambient conditions, making it difficult to isolate and characterize the ionic conductivity component and specifically, ionic mobility, which plays a critical role in controlling nanoionic device response times.[43]

The oxygen ion migration properties of metal oxides have primarily been studied at elevated temperatures. Owing to their thermally activated character, high temperatures are necessary to achieve sufficient conductivity to be readily and accurately measured, for example, by impedance spectroscopy. Furthermore, techniques enabling the separation of ionic and electronic contributions to the total conductivity generally rely on equilibration of the solid with the surrounding gas environment. Examples requiring reversible oxygen exchange at the surface of oxides to isolate oxygen ion conductivity, commonly limited to temperatures above ~500 °C, include Nernst concentration cells,[44,45] Hebb-Wagner polarization cells,[46–49] conductivity relaxation,[50–52] or isotope exchange followed by SIMS analysis[53–55]. Moreover, extrapolation of high-temperature data down to room temperature can be misleading due to enhanced defect-defect interactions, resulting in defect association and reduced defect kinetics.[56]

For thermal budget considerations, many of the materials used in nanoionic devices (e.g. memristors), such as binary and ternary metal oxides such as ZrO_2, Gd_2O_3, Ta_2O_5, HfO_2, SiO_2 or $SrTiO_3$,[31,57–60] are often prepared as undoped films, at reduced temperatures, and under vacuum conditions, leading to amorphous or polycrystalline films with ill-defined oxygen non-stoichiometries. Such materials are typically out of equilibrium with their growth conditions, implying an inexact knowledge of the existing defect concentrations, which can lead to significant variations in device performance.[43,61,62] Thus, an improved understanding and ability to control ionic defect concentrations, and resultant mobility in thin films, is vital in developing predictive models and improving device performance.

A general method for measuring bulk ionic mobility in MIECs was previously developed by one of the co-authors, termed *dynamic I-V analysis*.[63] The method is based on the examination of the non-linear current response of a thin film MIEC sandwiched between two electrodes upon application of triangular waveform voltage sweeps. The dynamic I-V analysis was recently applied to the MIEC model material, $Pr_{0.1}Ce_{0.9}O_{2-\delta}$ (PCO), defect chemical and transport properties of which were previously reported at high temperatures,[64,65] to characterize its oxygen vacancy mobility over wide temperature limits, extending down to near ambient conditions.[66] It was found that the migration enthalpy of oxygen vacancy mobility remains constant (0.82 ± 0.02 eV) between 35 °C and 500 °C. The corresponding oxygen vacancy mobility was measured to be 6.8×10^{-6} $cm^2V^{-1}s^{-1}$ at 500 °C, decreasing by seven orders of magnitude at 35 °C. While the absolute values of the oxygen vacancy mobility were in good agreement with those reported in the literature, it was noted that the migration enthalpy was 0.10 - 0.15 eV higher than expected. The two hypotheses put forward in that work to explain that behavior were: (1) defect association contributions could become important and contribute to the increased migration enthalpy for the considered temperature range measured, (2) the ionic migration enthalpy could be dependent on the local praseodymium dopant (Pr) oxidation state. We consider, that due to the mixed valence of the praseodymium dopant, $Pr^{4+/3+}$, its valence state in the prepared thin film device would be highly dependent on the history of the thermal and ambient treatment. Previously the Pr oxidation state was not quantitatively controlled and, in principle, could change during a wider temperature range study.[66] In this work, we investigate the oxygen vacancy mobility migration enthalpy as a function of the relative oxidation state of Pr in the mixed conducting regime of $Pr_{0.1}Ce_{0.9}O_{2-\delta}$. We focus on varying the oxidation state of Pr systematically, by exposing a single device to different intermediate temperatures anneals (400-600°C) under controlled oxygen partial pressure, followed by quenching-in the different

oxidation states. Taking advantage of the previously characterized optical properties of PCO,[67,68] we measured the optical transmission of the sample to extract the absorbance of the Pr^{4+} color center, and via knowledge of the defect chemical model that enabled quantification of the change in oxygen stoichiometry (δ varied in the range of 0.032±0.001 to 0.042±0.001). Furthermore, the oxygen vacancy mobility was measured, close to room temperature, by applying the dynamic I-V analysis method to PCO for the different determined oxygen vacancy concentrations. The fact that we use a single device, and perform our thermal annealing at medium temperatures, ensures that microstructural growth and cation segregation is minimized, enabling us to selectively probe changes in defect concentration and Pr oxidation state independent of other factors. This study contributes to the fundamental understanding of defect migration in mixed ionic-electronic conducting oxides and develops methods to probe their kinetics systematically under near ambient temperatures.

Method: Dynamic I-V analysis of Mixed Ionic-Electronic Conductors

Since in this manuscript we utilize a rather new methodology to probe the oxygen vacancy mobility, we first provide a brief review of the *dynamic I-V analysis* method employed in this study. The method is applied to a mixed ionic-electronic conductor placed between two ion blocking and electronically conducting electrodes in which the positively charged oxygen vacancies displace under an applied bias.[69] While the total concentration of oxygen vacancies, confined between the blocking electrodes, is designed to remain fixed, their net redistribution leads to the creation of oxygen vacancy depleted and enriched regions. This results in a redistribution of the electrons, attempting to maintain local charge neutrality, leading to a change in the overall conductivity, dominated by the

more mobile electronic species. For an MIEC with a prevailing electronic conductivity, the local depletion in oxygen vacancies leads to an increase in total resistance. In this configuration, an MIEC exhibits a non-linear behavior under sufficiently large applied voltages and sufficiently low frequencies.[69,70] A characteristic hysteretic shape with a peak current is exhibited due to a resistance change induced by the drift and redistribution of the positively charged oxygen vacancies. This response was previously modeled in detail by solving the electrically coupled ion and electron transport equations.[70] It was further demonstrated that the oxygen vacancy drift time through the length of the MIEC, can be determined from the time at which the peak current is reached, t_{peak}, for a given sweep rate, a_{SR}, of a periodic triangular waveform, as described in the following relation[63]

$$a_{SR}^{-1} = C\frac{\mu_i}{L^2}t_{peak}^2 \quad (1)$$

where μ_i is the ionic mobility, a_{SR} is the voltage linear sweep rate, L is the MIEC layer thickness, C is a dimensionless empirical constant, previously estimated to be equal to 2.[63] The parameter t_{peak} can either be experimentally determined by examination of the current vs. time plots or by dividing the applied voltage at the peak current by a_{SR}. Equation (1) is derived under two assumptions: (1) negligible in-series resistance of the electrodes and (2) linear voltage distribution inside the oxide. If condition (1) is not upheld, due to sufficiently resistive electrodes, then the effective voltage linear sweep rate in equation (1) will not be the same as the experimentally applied sweep rate used to determine the time-to-peak, as part of the voltage drop will be shared between the electrodes and the oxide. One can correct for the in-series resistance of the electrode by measuring their resistance separately (which can be temperature and oxygen partial pressure dependent). Assuming the electrodes have low resistance and do not exhibit voltage and sweep rate dependent changes in resistance over the sweep rate, voltage and temperature range studied, then the voltage per unit

time across the oxide will be equal to: $V_{oxide}(t) = V_{applied}(t) - R_{electrodes} \cdot I_{measured}(t)$ (See Figure S1 in SI). Importantly, Equation (1) does not explicitly depend on the ionic defect concentration nor on the type of ionic defect, e.g. doubly ionized oxygen vacancy, but that defect can be assumed for the model material $Pr_{0.1}Ce_{0.9}O_{2-\delta}$ that we use in this study.

Choice of Model Mixed-Ionic-Electronic Conducting Material: $Pr_{0.1}Ce_{0.9}O_{2-\delta}$

The method of *dynamic I-V analysis* was previously applied in measuring oxygen vacancy mobilities in $Pr_{0.1}Ce_{0.9}O_{2-\delta}$ (PCO), an MIEC thin film of interest as a cathode material in Solid Oxide Fuel Cells (SOFC). PCO is a mixed conducting system that crystallizes in the cubic fluorite crystal structure with a well-understood defect chemistry.[64,65] Pr is incorporated into the ceria cation sublattice being either isovalent Pr^{4+} relative to the host cerium cations, or, given its ability to be readily reduced, Pr^{3+}, serve as an acceptor dopant. The oxidation state of the Pr ion can be tuned from 3+ to 4+ by annealing at high temperatures in various oxygen-containing environments. The acceptor's negative relative charge is compensated by the generation of positively charged oxygen vacancies rather than holes. At these high dopant levels, the Pr levels form an impurity band situated ~1.4 eV below the conduction band,[64,68] enabling localized small polaron electron conduction within the Pr band. Close to room temperature, the total conductivity is expected to be dominated by electronic conduction within this band. Due to the small polaronic nature of the electronic carriers,[71] a maximum in conductivity is ideally expected when 50% of the Pr ions are 3+ and 4+ respectively, in which Pr^{3+} represents an electron localized on a Pr ion sitting substitutionally on a Ce site and Pr^{4+}, represents a nearby unoccupied Pr site.[64] Small polarons move via an activated hopping process in which a

localized electron can hop only to an adjacent unoccupied site. Most of our experimental results are in a regime for which Pr^{3+} is above 50% of the total Pr concentration.

Oxygen ion migration in PCO follows an oxygen vacancy hopping mechanism. The ionic mobility can be defined accordingly:

$$\mu_i = \mu_{i,0} \exp\left(-\frac{E_{m,i} + E_{as,i}}{k.T}\right) = \frac{\nu_{i,0}.a_0^2.q}{k.T}(1-c)\exp\left(\frac{\Delta S}{k}\right)\exp(-\frac{E_{m,i} + E_{as,i}}{k.T}) \qquad (2)$$

Where $\mu_{i,0}$ is the mobility prefactor composed of c, the site fraction of vacancies defined according to $\frac{[V_{\ddot{O}}]}{[V_{\ddot{O}}]+[O_O^x]}$, $\nu_{i,0}$ the attempt frequency, a_0 the jump distance, q the elemental charge and ΔS, the sum of activation entropy ΔS_a and configurational entropy ΔS_f. $E_{m,i}$ is the migration enthalpy and $E_{as,i}$ is the measured oxygen vacancy defect association energy. The effect of defect concentration in the pre-factor term $\mu_{i,0}$ of equation (2) is generally expected to result in a decrease in ionic mobility above the dilute limit (>1 atomic %).[72] At small concentration of defects, the site fraction c ~ 0 and therefore the ionic mobility is expected to be defect independent, while at higher concentrations, the site fraction results in a slight decrease in ionic mobility due to the reduced coordination of available lattice oxygen in the vicinity of the hopping vacancy.[72,73] The total ionic conductivity, which is proportional to the product of defect concentration and ionic mobility, is therefore typically expected to go through a maximum as a function of defect concentration due to the competition between the increasing carrier concentration and decreasing mobility due to defect association effects. More explicit details about the electronic and ionic behavior of PCO are described in SI.

Pr^{4+} is optically active allowing PCO to absorb sub band gap light in the range of ~ 450 - 750 nm[74]. The optical absorptivity, associated with the Pr^{4+} defect, can be controlled by varying the oxidation state of Pr, i.e., by shifting the oxidation state from 4+ to 3+, with the concentration of absorbing centers decreased. This was previously used by this group to characterize the oxidation state of the Pr ion, and in turn, with the aid of a well-understood defect chemical model, correlate this to the oxygen vacancy concentration.[67]

Experimental

Sample preparation of PLD targets for thin film deposition

The PCO PLD target was synthesized using a powder prepared by a co-precipitation procedure described by Spiridigliozzi et al.[75] Cerium nitrate $Ce(NO_3)3{:}6H_2O$, and praseodymium nitrate $Pr(NO_3)3{:}6H_2O$ (Strem chemicals) {99.99%}, in stoichiometric proportion (90/10), were dissolved in distilled water at a concentration of 0.1 $molL^{-1}$. The precipitation solution was prepared by dissolving ammonium carbonate in distilled water at a concentration of 0.5 $molL^{-1}$. The amount of ammonium carbonate solution was calculated to have a molar excess of 2.5 as compared to the total amount of cations in the nitrate solution. The ammonium carbonate solution was poured into the vigorously stirred nitrate solution to trigger precipitation. The precipitate was subsequently filtered and washed four times in distilled water in a Buchner filter connected to a vacuum pump and dried at 100 °C overnight, followed by calcination at 600 °C for 1 h with 2 °C/min heating and cooling rate to obtain the PCO oxide powder crystallized in the fluorite structure. The powder was subsequently pressed into a 30 mm diameter disk with a uniaxial press (1000 $kg.cm^{-2}$), and sintered at 1500 °C for 6 h, followed by cooling at 1 $°Cmin^{-1}$ to prevent crack formation, yielding a pellet with 97 % density (theoretical density of 7.2 $g.cm^{-3)}$. In_2O_3/SnO_2 90/10 wt % (ITO) transparent conducting electrodes were prepared from a 1 inch commercially purchased PLD target from Kurt J. Lesker Company with a purity of 99.99% (theoretical density of 7.14 $g.cm^{-3}$).

Crossbar ITO/PCO/ITO thin film devices

To determine the PCO oxygen vacancy mobilities by the dynamic I-V analysis, crossbar devices with ITO electrodes were prepared. First, a bottom ITO electrode, 100 nm thick, 2 mm long, and 300 µm

wide bar with a contact pad, was patterned through a shadow mask onto an Al_2O_3 single crystal (0001) oriented (c-plane) substrate (Crystec GbmH, Germany). Next, a 1mm square-shaped ~300 nm thick PCO thin film was grown on top of the bottom ITO electrode. Both the ITO and PCO were grown by PLD with the parameters given below. After a base pressure of $7 \cdot 10^{-6}$ mbar was reached, pure oxygen was constantly leaked into the PLD chamber, keeping the total pressure at 0.013 mbar during film growth and cooling steps. During the deposition, the substrate temperature was held at 250 °C (heating and cooling rates were 10 °C/min), and the target to substrate distance was 7.5 cm. The laser energy was set to 150 mJ resulting in a power density of about 1.5 $J \cdot cm^{-2}$. The resultant PCO film formed a continuous layer on the Al_2O_3 substrate and the bottom ITO electrode. Finally, a top ITO electrode was grown by PLD at 250 °C onto the PCO thin film using a similar shadow mask as the bottom electrode rotated by 90°. The active area is given by the intersection of the bottom and top electrodes, i.e. a square with 300 µm sides, where the PCO thin film is sandwiched between the ITO electrodes. The X-ray diffraction patterns of the thin films were measured with the Rigaku SmartLab with a Cu Kα rotating anode source in a coupled scan and a rocking curve. Images of the cross-sections of the device were acquired on a Zeiss Merlin high resolution scanning electron microscope.

Oxygen non-stoichiometry control and quantification by optical measurements in PCO

The oxygen content of the devices, δ, was modified by heating the PCO film in different oxygen partial pressures at intermediate temperatures (400-600 °C) for a fixed amount of time, followed by rapid quenching to freeze in the respective defect concentrations. This was performed in a single device to rule out possible differences related to microstructure, or

cation segregation towards surfaces or grain boundaries. The chosen temperature range ensured surface limited oxygen exchange kinetics (see Figure S2 in SI), leading to a homogenous distribution of oxygen vacancies in the film throughout the annealing process.[67,76] The sample was heated under different oxygen partial pressures in the pO_2 range from $1x10^{-21}$ – 1 atm (using different mixtures of Ar and O_2 mixture, and a dilute mixture of 100 ppm H_2 in Ar buffered in 3% H_2O). The exact conditions are summarized in Table 1 in the SI. The oxygen content in the PCO film was optically tracked by measuring the change in visible light absorption with a broad peak at around 532 nm, correlating with the concentration of Pr^{4+} ions.[67,76]. After the sample was cooled down to room temperature, full wavelength transmission spectra were measured, 350-900 nm, to evaluate the new quenched-in oxygen vacancy concentration. Specifically, the new oxygen vacancy concentration can be estimated by calculating the absorption coefficient from the transmission spectra and applying the Beer-Lambert law to estimate the Pr^{4+} concentration (as described in optical measurement in SI) which is then equated to the new oxygen vacancy defect concentration via the correct defect chemical equilibria relation.[65] The strength of this technique lies in the fact that it provides a non-contact, non-destructive method for quantifying the oxygen vacancy concentration on both a relative and absolute scale. For the optical measurements, a dual-beam spectrophotometer, customized to enable in-situ (in furnace) measurements of the total optical transmission in a UV-VIS-NIR wavelength range with 2 nm wavelength resolution, was utilized. The incident beam originated from a Newport Apex Illuminator 70613NS with monochromator 74100 to obtain a continuous optical transmission spectrum. A monochromatic light beam (2 nm linewidth) was passed through the samples positioned within a quartz cell installed inside a furnace heater. A beam splitter was used to direct part of

the incident beam to a reference sample (bare Al_2O_3 substrate) positioned next to the sample in the optical cell, which allowed for the removal of variations in the light source intensity, and artifacts as the beam passes through the quartz tube and substrate. To improve the signal-to-noise ratio, the incident beam was mechanically chopped at constant frequency and then measured using a lock-in amplifier (SRS, model SR830).

Studying the local bonding near order changes with non-stoichiometry by Raman spectroscopy

Raman spectroscopy was employed to study the Raman vibrational modes of oxygen-cation bonds as a function of oxygen non-stoichiometry to assess changes in bond lengths and changes due to defect association. The Raman measurements were performed on the backside of the PCO PLD target and on a separate 200 nm PCO film grown on 100 nm ITO deposited on a single crystal (0001) oriented (c-plane) Al_2O_3 substrate using similar conditions as the film used during the mobility studies. The film was also exposed to similar annealing procedures to quench in varying degrees of non-stoichiometry (see Figure S5 in SI). A Renishaw Invia Reflex Micro Raman was employed with a 100 x objective yielding a 1 micron spot size, spectral resolution of a ± 0.5 $cm^{-1,}$ and laser power of 1 mW. An excitation wavelength of 783 nm (1.58 eV) was selected based on the need to avoid electronic resonance both in the Pr optical sub-band or the Ce optical band gap. The data was analyzed by fitting the peak curves and subtracting the baseline to remove the background. The data was then normalized by the highest peak intensity. Fitting was done by OriginPro 9.0G using a Lorentzian function for the F_2g peak and Gaussian for all others.

Investigating changes in ionic defect conductivity and mobility by electrical characterization

Two different types of electrical measurements were utilized. 1) I-V curves were used to extract ionic mobility by application of high amplitude (1.5 V) triangular voltage waveforms onto the thin film crossbar device with sweep rates ranging from 1 to 500 mVs^{-1} for the dynamic I-V analysis of the ionic mobility. 2) Electrochemical Impedance Spectroscopy (EIS) spectra were measured before and after each set of I-V measurements, utilizing low amplitude sinusoidal voltages (10 mV) in the frequency range of 1 to 10^6 Hz with spectra fitted to obtain equivalent R and C circuit elements with the aid of Zview software (Scribner Associates). The electrical measurements on the PCO crossbar were performed in a temperature and atmosphere-controlled microscopy/spectroscopy stage (Linkam Scientific Instruments). The samples were contacted by spring-loaded stainless-steel needles directly on the device contact pads. Measurements were performed with a potentiostat (Solartron Analytical, ModuLab XM ECS) outfitted with a frequency response analyzer module (XM MFRA).

Results

Figure 1a shows a schematic cross-section of the structure and a top optical micrograph view of the prepared ITO/PCO/ITO device. Figure 1b shows the SEM cross-sectional image of the as-prepared PCO thin film grown by PLD on an (0001) oriented (c-plane) Al_2O_3 substrate. A columnar textured structure of PCO film is visible with grain sizes on the order of 68 ± 18 nm. Figure 1c shows a Grazing

incident XRD pattern of a similarly grown columnar textured structure film by PLD. By comparison with a reference $Pr_{0.1}Ce_{0.9}O_{2-\delta}$ pattern, the film is seen to be polycrystalline.

In-situ control and optical measurement of PCO oxygen non-stoichiometry in thin-film crossbar device

To vary the oxygen non-stoichiometry, we heated the thin film sample in different oxygen containing atmospheres and then quenched-in different non-equilibrium stoichiometries. Figure 2a schematically summarizes the quench-in procedure, depicting the expected different regions of the total conductivity σ_{tot} as a function of $\log(pO_2)$ at 50 °C following the different annealing steps, keeping in mind the maximum conductivity expected at $[Pr^{3+}] = [Pr^{4+}]$ for small polaron transport. When varying the oxygen non-stoichiometry, the total conductivity of PCO close to room temperature is expected to be dominated by its electronic conductivity and to vary according to small polaron behavior, as described in the SI. The optical transmission spectra measured were used to measure the level of oxidation/reduction of the PCO thin film. Figure 2b shows the optical transmission spectra of the crossbar device over the wavelength range of 350-900 nm measured after quenching the sample to room temperature from the different annealing steps. The minima in the optical transmission spectrum, do not relate directly to absorption peaks but arise from the constructive and destructive interference of the incident light beam with back reflected beams from the thin film – substrate interface resulting in the observed patterns (see optical measurement in SI). For a constant refractive index and thickness, the interference patterns are not expected to change intensity or position. Samples quenched from more reducing environments show higher transmission in the 400-800 nm region, whereas samples annealed in oxygen show lower

transmission. All transmission curves of samples annealed in different environments converge above 800 nm, consistent with the fact that there is no color center absorption at those higher wavelengths.

Studying local bonding near order changes with stoichiometry by Raman spectroscopy

To probe changes in lattice parameter, we focused on the main Raman mode of ceria with F_{2g} symmetry, known as the symmetric oxygen breathing mode around the Ce cation, which enables tracking bond length changes between O-Ce-O.[77] Figure 3a shows the Raman spectra recorded using a 783 nm wavelength for a similar 200 nm $Pr_{0.1}CeO_{2-\delta}$ sample grown on ITO/Al_2O_3 substrate and exposed to similar annealing as the sample prepared for mobility measurements. The oxygen non-stoichiometry in this Raman study was found to vary from 0.035±0.001 to 0.042±0.001 from the most oxidized sample to the most reduced sample, respectively, according to the recorded optical transmission spectra (see Figure S5 in SI). One observes a major common peak at 460 cm^{-1} in all four spectra consistent with the oxygen breathing mode around the Ce^{4+} cation with F_{2g} symmetry and two defect-related peaks around ~550/600 cm^{-1}. These defect peaks have generally been associated with the presence of the dopant ions and oxygen vacancies, but their exact origin remains a source of debate.[77] The peak at ~550 cm^{-1} has been shown to exist only when oxygen vacancies are present in the system and is therefore considered a fingerprint for the latter. Moreover, the peak at ~600 cm^{-1} has been shown to be activated by the presence of aliovalent dopants and was hypothesized to originate from the F_{1u} (LO) phonon mode, usually only IR active, becoming Raman active due to the local lattice distortion relaxing symmetry rules.[77] Furthermore, by examining the relative peak heights under resonant condition in Pr doped CeO_2,[78] it was shown that the ~600 cm^{-1} band could be

related to the presence of the optically active Pr^{4+} cation. In that case, the peak height of the defect peak at ~550 cm^{-1} and ~600 cm^{-1} relate to each other as the former relates to the presence of oxygen vacancies introduced by the aliovalent Pr^{3+} while the latter is associated with the presence of Pr^{4+} and the sum of the two concentrations must be constant. As seen in Figure 3b, the F_{2g} peak (at 460 cm^{-1}) does not shift position within a resolution limit of ±0.5 cm^{-1} while its full-width half max (FWHM) increases from 22 cm^{-1} to 26 cm^{-1} as the sample oxygen non-stoichiometry was increased, suggesting the onset of defect association and ordering due to the formation of additional nonsymmetric bonding symmetry. As seen in Figure 3c, the peak height at ~550 cm^{-1} increases while the peak at ~600 cm^{-1} decreases as the sample oxygen non-stoichiometry is increased. Additionally, for the two most reduced samples, there is a sign of a peak at ~250 cm^{-1} which indicates a local symmetry reduction enabling Raman activity of additional F_{1u}(TO) phonon modes normally prohibited by symmetry rules and used as a fingerprint of local lattice distortion and the onset of defect association. The broad peak contribution at ~200 cm^{-1} was present in all films and also in the PCO pellet (see figure S7). We are not certain about the source of this peak in PCO as it has not been reported in the Raman spectra literature for ceria, althought it seems to be characteristic of the prasodymium doping in the ceria solute solution. However, because it did not change in position or in character through our different thermal anneals indicating its invariance, it was therefore excluded from the Raman analysis. Additionally, the sharp peak contributions at 376 cm^{-1}, 416 $cm^{-1,}$ and 577 cm^{-1} could be assigned to the underlying ITO and are therefore excluded from the PCO Raman analysis and further discussion (see Figure S6 in SI).

Electrical Conductivity Measurements of PCO Thin Film Crossbar Devices

Figure 4a shows examples of EIS measurements made on the ITO/PCO/ITO device over the temperature range of 50 to 100°C at 10°C intervals prior to the dynamic I-V measurements. Each

data point represents a different frequency with frequency increasing from high to low Z' values. The table inset in Figure 4a lists the frequency at the peak (maximum Z") of each semicircle. An impedance spectrum was taken for each frozen-in stoichiometry at a series of temperatures. An equivalent circuit, as represented in the inset of Figure 4a, was employed to analyze the response of the sample in which R1 represents the series resistance of the electrodes given by the offset resistance of the semicircle from the origin, R2 and CPE2 represent the bulk PCO equivalent circuit given by a resistance and constant phase element in parallel as reflected in the main semicircle, and R3 and CPE3 represent a similar circuit representing the interfacial electrode contributions as reflected in the small partial semicircle originating at the low-frequency end of the major semicircle. CP4 in parallel to R2//CPE2 and R3//CPE3 , represents the stray capacity that very likely originates from the Al_2O_3 substrate. (Further details on the choice of the equivalent circuit model is provided in the supplementary) Figure 4b shows an Arrhenius plot of the bulk (R2), largely electronic conductivity (i.e. $\sigma_{bulk} \sim \sigma_e$), $log_{10}(\sigma_e.T)$ vs $1/k_bT$, for the different non-stoichiometric states of the device. The derived activation energies vary from 0.36 ± 0.01 eV for the most oxidized sample (δ~0.032±0.001) to 0.51 ± 0.01 eV for the most reduced sample (δ~0.042 ± 0.001). Linear fitting to these data yields $\sigma_{e,0}$= 28.19 ± 1.1 S.cm^{-1} for the most oxidized sample (δ~0.032 ± 0.001), $\sigma_{e,0}$= 61.16 ± 1.1 S.cm^{-1} for the partially oxidized sample (δ~0.035 ± 0.001), $\sigma_{e,0}$= 130.02 ± 1.2 for the as-prepared sample (δ~0.039±0.001) and $\sigma_{e,0}$= 321.12 ± 1.2 S.cm^{-1} for the most reduced sample (δ~0.042±0.001). The conductivity, σ_e, of the most oxidized sample (δ~0.032), 1.16x 10^{-4} S.cm^{-1}, is ~17 x higher than the conductivity of the most reduced sample (δ~0.042), 6.64 x 10^{-6} S.cm^{-1}, at 60 °C consistent with the trend represented in Figure 2a where we positioned the conductivity data to fall on the p-side (left) of the small polaron conductivity maximum as a function of pO_2.

Dynamic I-V Analysis of Ionic Mobility in PCO Thin Film Crossbar Devices

Figure 5a shows an example of the dynamic non-linear I-V response of a PCO crossbar device with δ~0.032 ± 0.001, measured at 60 °C as a function of applied voltage sweep rate, corrected for the electrode resistance contribution. The I-V curve exhibits hysteresis and characteristic current peaks at both positive and negative voltage polarities (occurring at a time t_{peak}). The range of the sweep rates leading to the hysteretic I-V response and current peaks was experimentally determined for a peak voltage amplitude of 1.5 V. Figure 5b shows a plot of reciprocal sweep rate, a_{SR}^{-1}, versus time-to-current-peak squared, t_{peak}^2. The dependency is observed to be linear, as predicted by Equation (1). The slope of the fitted line, calculated from Equation (1), is used to find the corresponding ionic mobility, 1.46 ± 0.04 x10^{-12} $cm^2V^{-1}s^{-1}$, corresponding to a diffusivity of 4.20 ± 0.16 x10^{-14} cm^2s^{-1} by application of the Nernst-Einstein relation. Figure 5c shows an Arrhenius plot of $\log_{10}(\mu_i T)$ vs. $1/k_b T$ for the as-prepared sample. The activation energy, $E_{m,i} + E_{as,i}$, as defined in equation (2) , for the oxygen vacancy mobility equals 0.73 ± 0.04 eV over the temperature range from 50-100 °C, while the y-axis intercept yields $\mu_{i,0}$= 41.5 ± 1.7 $cm^2V^{-1}s^{-1}$.

Figure 6a shows an Arrhenius plot of $\log_{10}(\mu_i T)$ vs. $1/k_b T$ for the PCO film for the different quenched-in stoichiometries. The as-prepared sample (δ ~ 0.039 ± 0.001) exhibited a migration enthalpy of 0.79 ± 0.02 eV. Reduction of the film (δ ~ 0.042 ± 0.001) leads to a similar energy of 0.79 ± 0.02 eV, while oxidation (δ ~ 0.035 ± 0.001 and 0.032 ± 0.001) led to smaller activation energies of 0.74 ± 0.01 eV and 0.73 ± 0.04 eV, respectively. The intercepts vary from $\mu_{i,0}$= 5589.9 ± 1.8 $cm^2V^{-1}s^{-1}$ for the most reduced sample (δ ~ 0.042 ± 0.001) to $\mu_{i,0}$= 41.5 ± 4.3 $cm^2V^{-1}s^{-1}$ for the most oxidized sample (δ ~ 0.032 ± 0.001). Figure 6b shows the ionic mobility as a function of δ for temperatures

from 50-100 °C. With knowledge of the film thickness and literature values for the extinction coefficient of Pr^{4+} in $Pr_{0.1}Ce_{0.9}O_2$,[67] for a given wavelength (λ~532nm) at room temperature, $\varepsilon_{Pr^{4+}}$= 5.01 ± 0.14 x 10^{-18} cm^{-2}, we estimate the concentrations of Pr^{4+} ($[Pr_{Ce}^{x}]$) and Pr^{3+} ($[Pr_{Ce}^{\prime}] = [Pr_{Ce}^{total}] - [Pr_{Ce}^{x}]$) which according to the PCO defect model, can be correlated to the oxygen vacancy concentration via the electroneutrality relationship $[Pr_{Ce}^{\prime}] = 2[\ V_O^{\cdot\cdot}]$. The sample non-stoichiometry, δ, was varied from 0.032 ± 0.001 to 0.042 ± 0.001 (Δδ ~ 0.01). At each temperature, the factor μ_i.T shows a linear dependence on concentration with slopes varying from 2.15 ± 0.4 x 10^{-7} to 1.07 ± 0.1 x 10^{-5}, while the intercept shows an increase from -6.38 ± 1.6 x10^{-9} to -3.31 ± 0.36 x10^{-7} .

Discussion

Previously reported values of the oxygen vacancy mobility in $Pr_{0.1}Ce_{0.9}O_{2-\delta}$, derived by the dynamic I-V analysis for a single nominal value of δ,[79] were found to be in a good agreement with those from the literature for ceria based oxygen conductors.[61,65,80] However, it was noted that the activation energies derived from the dynamic I-V analysis were 0.10 - 0.15 eV higher than those reported previously for acceptor doped ceria-based compounds. It was proposed that the differences in migration enthalpy could be due to defect association, more dominant at lower temperatures, or due to possible influences of defect concentration on ionic mobility.[79] In the present study, we show that the ionic mobility in $Pr_{0.1}Ce_{0.9}O_{2-\delta}$ is indeed significantly dependent on defect concentration at low temperatures, with observed changes in both the migration enthalpy and pre-factor. For example, the mobility was observed to increase by a factor of 13 at 60 °C from 1.46 ± 0.09 x 10^{-12} $cm^2V^{-1}s^{-1}$ to 1.92 ± 0.03 x 10^{-11} $cm^2V^{-1}s^{-1}$, while the migration enthalpy exhibited an increasing trend

(average rise from 0.73 ± 0.04 eV to 0.79 ± 0.02 eV), as the oxygen vacancy concentration was increased by from δ ~ 0.032 ± 0.001 to 0.042 ± 0.001 (see Figure 6a). The mobility pre-factor varied by a factor of 134 x from $\mu_{i,0}$= 5589.9 ± 1.8 $cm^2V^{-1}s^{-1}$ for the most reduced sample (δ ~ 0.042 ± 0.001) to $\mu_{i,0}$= 41.5 ± 4.3 $cm^2V^{-1}s^{-1}$ for the most oxidized sample (δ ~ 0.032 ± 0.001). A priori, this is surprising as the majority of reports in the literature on acceptor doped CeO_2 show no change or a decrease in the ionic defect mobility with increasing defect concentration.[72,81]

Considering first the change in migration enthalpy, it is known that nominally undoped ceria has an ionic mobility migration energy of around 0.6 eV and therefore it is consistent to find that the migration enthalpy of ~ 0.73 ± 0.04 eV for the oxidized Pr doped sample (i.e. with low oxygen vacancy concentrations), approaches that value.[61] This is also in line with previous experimental measurements on $Pr_xCe_{1-x}O_{2-\delta}$ that showed migration enthalpies ranging from 0.66 to 0.84 eV for *x* values from 0.008 to 0.20.[65] The upper migration enthalpy value of 0.79 ± 0.02 eV obtained in this study, as well, approaches the upper limits of those measured in the literature of ~ 0.9 eV. The increase in migration enthalpy with defect concentration is consistent with an increased vacancy – vacancy-dopant defect interactions as reported by Koettgen et al.[61] who examined the relationship between defect association at the microscopic level and the macroscopic oxygen ion conductivity in doped ceria by combining ab initio density functional theory (DFT) with Kinetic Monte Carlo (KMC) simulations, calculating the maximum in oxygen ion conductivity as a function of dopant concentration. By considering trapping and blocking phenomena, they were able to simulate the experimentally observed maxima in ionic conductivity as a function of doping concentration for various acceptor doped ceria compounds. Trapping and blocking were defined for the cases where

the migration barrier for oxygen vacancy hopping towards and away from a dopant were asymmetrically or symmetrically modified by doping, respectively. The main conclusion from their study was that while the simulated apparent activation enthalpies at low dopant fractions are equal to the migration energy, the activation enthalpy increases with increasing dopant fraction caused by the interactions between defects dominated by the trapping behavior. This picture is consistent with the results of our Raman measurements over a similar stoichiometry range of $\delta \sim 0.035 \pm 0.001$ to 0.042 ± 0.001, as seen in Figure 3. The lack of significant F_{2g} peak splitting, the existence of the F_g double fluorite band at 370 cm^{-1} over the entire oxygen non-stoichiometry range and the existence of the 250 cm^{-1} F_{1u} (LO) for the two most reduced stoichiometries, indicates that the oxygen vacancies in our material system are partially associated, but have not yet formed a long range ordered structure (see Raman analysis in SI for details). As more Pr ions are reduced to 3+, more oxygen vacancies are introduced into the lattice, and trapping around the Pr^{3+} cations becomes stronger, resulting in a higher degree of defect–dopant interactions, contributing to the increase in association energy. This dependence of the association energy with Pr^{3+} and oxygen vacancy concentration can explain the dependence of the oxygen vacancy migration enthalpy on the oxidation state of the Pr ion.

The model developed by Koettgen et al.[61] fails, however, to describe the dependence of the pre-factor of ionic mobility on defect concentration observed in this study as they predicted a nearly constant attempt frequency in the mobility pre-factor, independent of defect concentration. A similar dependency of the ionic mobility pre-factor on oxygen vacancy concentration, as observed in this study, was previously reported by Nguyen et al.[82] in acceptor doped $LaAlO_3$, a wide band gap

semiconductor whose dominant mobile ionic defect are also oxygen vacancies. Here we note that while analogies to this system in comparison with ours (PCO) may be limited due to fundamental differences in crystal structure (fluorite vs distorted perovskite) and dominant defect type (anion Frenkel vs Schottky disorder), insights may still be gained in terms of the possible origins of the observed phenomena. It was observed that the ionic mobility increased with increasing defect concentration until a maximum was reached, at which point the oxygen vacancy mobility began to decrease. The activation energies increased with increasing defect concentration until the pO_2 independent ionic plateau was reached. In our case, we notice in Figure 4b and Figure 6a that when the sample is most heavily reduced ($\delta > 0.05$), past the ionic plateau regime into the Ce^{3+} reduction regime (see SI for details), the ionic mobility passes through a maximum and exhibits a migration enthalpy of 0.74 ±0.02 eV and pre-exponential factor equal to 230.6 ±1.6 $cm^2V^{-1}s^{-1}$ (see Figure 6). To discuss the possible sources contributing to the changes in ionic mobility (μ_i) and its pre-factor ($\mu_{i,0}$) with defect concentration observed in this study, we examined the effects of strain, ambipolar diffusivity, and entropic configuration. As described in the supplementary, we can rule out the effect of strain on the observed trend as the Raman data Figure 3 confirms a nearly invariant lattice parameter with defect concentration. Likewise, the expected ambipolar diffusivity behavior cannot explain the observed trend as the ionic diffusivity would follow the small polaron mobility, which in this case, is decreasing with increasing defect concentration.

We, therefore, focused our attention on the potential impact of changes in the entropic configuration on oxygen vacancy mobility associated with oxygen non-stoichiometry changes. As discussed above, one usually observes a correlation between decreasing oxygen vacancy mobility

with increasing migration enthalpy in CeO_2 based acceptor doped solid electrolytes. This is attributed to increased fractions of oxygen vacancies trapped in the vicinity of charged dopants as the dopant concentration increases.[61] The transition from the trapped to the detrapped state in weakly doped ceria (~1-5%) generally occurs around 300-400 °C.[56,83] The results of our measurements are counterintuitive with respect to this picture, given the simultaneous increase in both the migration enthalpy and the pre-factor of the ionic mobility. To discuss the question of the potential impact of changes in the entropic configuration on oxygen vacancy mobility, it is useful first to examine the discussions surrounding the so-called Meyer-Neldel law that describes materials that display a linear dependence between $\log_{10}$ ionic conductivity, pre-exponential factor, and migration enthalpy.[55]

As seen in Figure 6c, our data exhibits, within the statistical error of the measurements, a positive linear dependence between the pre-exponential factor and migration enthalpy, consistent with the Meyer-Neldel behavior. The Meyer-Neldel law is almost universally obeyed, for example, by semiconductors that are disordered or inhomogeneous in some manner.[84] Two phenomenological models have been put forward for ionic conductors to describe their behavior.[85,86] The first is based on adopting a random walk model and assuming random spatially varying activation energies for jumps with an exponential probability distribution. The second model is based on the idea of freezing-in defects where the pre-exponential term reflects the temperature at which the defect concentration is frozen in.[86] Similarly, the Meyer-Neldel law has been used to explain changes in migration enthalpy and pre-exponential factor in glass ceramic conductors for which a distribution of free volumes with different percolative paths are quenched in.[84] The migration enthalpy is not as sensitively dependent on this distribution of paths compared to the configuration entropy, as the

former reflects the average energy for *mobile* ion migration. In contrast, the latter reflects all the possible configurations and pathways. The second model concept related to the freezing in of defects does not satisfactorily explain the observed trend, as expressed in equation (2), a change in defect concentration would only be expected to lower the mobility of ionic defects due to a reduced site fraction of available lattice oxygen for the oxygen vacancy to hop into. On the other hand, the concept of spatially varying activation energies for jumps with an exponential probability distribution and percolative pathways is of interest as similar analogies can be drawn with that of a distribution of defect associates in our system.

Examples in the literature of the latter resulting in changes in the pre-exponential factor of the oxygen vacancy ionic conductivity have been made in various *stabilized zirconia systems.*[87,88] For example, in the case of $Ca_xZr_{1-x}O_{2-x}$,[89] the ionic mobility of oxygen vacancies could be substantially decreased by isothermally holding the sample ~1000 °C for several hours. This change in conductivity was attributed largely to a pre-exponential factor change as the migration enthalpy was nearly invariant and was attributed to a process of cations ordering with oxygen defects in the system. This has often been reported as an aging phenomenon for samples held >1000 °C for 100's hours.[83,87,88,90,91] These phenomena were shown to result from significant changes in the lattice structure via the formation of *micro-domains*.[91] For samples annealed at a much higher temperature (>1600°C), the disorder in the system could be recovered, while for samples annealed below 650°C, owing to the extremely slow migration kinetics of the cations, did not show any ordering. When discussing the origin of defect association as a function of temperature, we must recognize that the

nature of forming defect complexes is dependent on the temperature at which the sample is annealed.

It is generally accepted that at low temperatures, when we consider defect association between oxygen vacancies and trivalent dopants, the latter are considered immobile and, therefore, only the former (i.e. mobile oxygen vacancies), order themselves around the cations. This tends to result in partially compensated defect dipoles, that in the case of PCO would be given by[92]

$$Pr'_{Ce} + V_{\ddot{O}} \leftrightarrow (Pr'_{Ce}\, V_{\ddot{O}})^{\cdot} \quad (3)$$

At higher temperatures, typically above ~1000 °C, cations, as well, become mobile undergoing an ordering process along with the mobile oxygen vacancies. This would result, in the case of PCO in the formation of neutral defect tripoles, given by[92]

$$2Pr'_{Ce} + V_{\ddot{O}} \leftrightarrow (2Pr'_{Ce}\, V_{\ddot{O}})^{x} \quad (4)$$

The migration kinetics of the two complexes are expected to be different, with an oxygen vacancy more strongly *trapped* in the neutral tripole as compared to that in the dipole. Starting from a disordered state, depending on the annealing temperature and time, different distributions of dipoles and tripoles can be expected to form in the lattice. Owing to lower dissociation energetics, oxygen vacancies will prefer to migrate along dipoles rather than tripoles. Thus the overall migration kinetics of oxygen vacancies would be expected to follow a percolated network of dipoles. The presence of tripoles is expected to *constrict* the pathways through which the oxygen vacancy can migrate, by limiting the different dipolar pathways available for the migrating oxygen vacancy to follow, thus resulting in lower migration entropy and, therefore a lower ionic mobility pre-factor.

We note that a major difference between the conventional fixed valent and our mixed valent doped system is that the extra negative charge on the compensating cation in the PCO system, Pr^{3+}, is mobile. The diffusivity of Pr ions is expected to be similar to that of Ce ions and other rare earth cations of similar valence, which only become mobile at temperatures >1000 °C (diffusivity of 10^{-14} - 10^{-18} cm^2s^{-1} from 400-600°C)[93–95] and therefore would not be sufficiently mobile during our temperature treatment to rearrange into micro-domains. However, the high mobility of the small polaron (diffusivity of 10^{-5}- 10^{-6} cm^2s^{-1} between 400-600°C)[64,65] could readily enable it to undergo ordering at reduced temperatures, leading to the formation of neutral tripoles as described in equation (4) as well as dipoles in the temperature range of 400-600°C. The temperature range employed in this study coincides well with values reported in the literature for the temperature onset of defect association in ceria or zirconia (~300-400 °C)[56,83,96], which generally refers to dipole formation. In preparing our specimens, the different thermal/atmosphere treatments used to achieve different levels of stoichiometry were likely to have quenched in different levels of neutral tripoles and charged dipoles. For the sample annealed at rather elevated temperatures (δ ~ 0.042), this could result in a rather minimal formation of neutral tripoles, and thus a high pre-exponential factor due to a highly disordered Pr^{3+} sublattice. In contrast, the samples held longer at lower temperatures under oxidizing conditions (δ ~ 0.032 & 0.035) could lead to the partial formation of neutral tripoles resulting in narrower conduction pathways for mobile oxygen vacancies. We provide a schematic representation of the ordering concept for a fixed non-stoichiometry in Figure 7. The different stoichiometries achieved by thermal annealing and the impact on the small polaron mobility would likely shift the transition temperature for neutral tripole formation. Ultimately, the presence of tripoles (the maximum possible amount of tripoles vs dipoles) in the lattice will reflect

the conditions under which the film was grown and the physical distribution of Pr ion in proximity of each other. Further experimental and modeling efforts are required before a more exact explanation for the source of the steep change in mobility pre-factor with different annealing times/temperatures and increasing defect concentration can be established.

Summary and Conclusions

In this study, we quantitatively demonstrated, in a single device, that varying the oxygen vacancy concentration can have a significant impact on the magnitude of ionic mobility and its migration enthalpy, thus demonstrating the importance of considering the effect of defect concentration on ionic mobility in these MIEC through directed experimental efforts. The existence of an interband gap optical absorption center in the model $Pr_{0.1}Ce_{0.9}O_{2-\delta}$ (PCO) system, associated with the oxidation state of the Pr ion, was leveraged to monitor changes in film oxygen non-stoichiometry. By processing the ITO/PCO/ITO crossbar device at elevated temperatures in ambients with different pO_2's, it was possible to quench-in to room temperature different degrees of oxygen non-stoichiometry (δ) varying from 0.032 ± 0.001 to 0.042 ± 0.001 as quantified by optical absorption measurements. By combining this information with mobility data extracted from dynamic IV analysis of an ITO/PCO/ITO crossbar device, insight was gained into the impact of non-stoichiometry on ionic mobility near room temperature. A linear dependence of ionic mobility on defect concentration was found. For increases in oxygen vacancy concentration as low as 20% (corresponding to Δδ ~ 0.01), the mobility increased by up to 13-fold, while its migration enthalpy exhibited a weak but positive dependence on nonstoichiometry ranging from 0.73 ± 0.04 eV to 0.79 ± 0.02 eV). with increasing

nonstioichiometry. While a general increase in migration enthalpy with increasing defect concentration would be consistent with reports of increasing defect association with increasing defect concentrations in acceptor-doped ceria, the increase in the ionic mobility pre-factor of up to 13-fold was not. Strain, defect association, ambipolar diffusivity, and configurational entropy were all considered as possible factors in attempting to explain this trend. Raman spectroscopy results served to rule out changes in strain as primary causes for the large increases in mobility. The small polaron behavior of electronic charges in PCO, as examined by impedance spectroscopy, was inconsistent with the possible role of ambipolar transport in explaining this surprising result. On the other hand, the positive correlation between migration enthalpy and pre-exponential factor was observed to follow a Meyer Neldel like behavior. Variations in configurational entropies associated with the quenching procedure utilized in this study, coupled with the unusual nature of the acceptor dopant supporting migration via electron hops between occupied Pr^{3+} ions and neighboring empty Pr^{4+} ions, was hypothesized to lead to a distribution of percolated transport pathways. Further experimental and modeling efforts are required before a more exact explanation for the source of the steep change in mobility pre-factor with different annealing times/temperatures and increasing defect concentration can be established.

This study offers valuable insights for a variety of nanoionic devices operating under near ambient conditions, where knowledge about the as-prepared non-stoichiometry is generally lacking. Significant differences in room temperature ionic mobility and electronic conductivity, as well as varying activation energies, can result in large discrepancies in device operations. Moreover, the presence of inhomogeneous defect migration pathways through a percolated network of defect

clusters could have significant implications, for example, on the variability of memristive devices that rely on the formation of nanometric sized ionic defect filaments. Pathways of high ionic mobility would likely be key candidates for the nucleation and propagation of such filaments. Moreover, this methodology offers the opportunity for future systematic examination of the impacts of different stimuli e. g. high field or strain, on ionic mobility in mixed ionic-electronic conductors at reduced temperatures.

Supporting Information

Supporting Information is available from the Wiley Online Library or from the author.

Acknowledgments

TD, DK and HLT thank the U.S. Department of Energy, Basic Energy Sciences Program: "Chemomechanics of Far-From-Equilibrium Interfaces" (COFFEI), project DE-SC0002633 for funding. This work was also supported for JLMR and TD by the MRSEC Program of the National Science Foundation under award DMR-1419807. This work made use of the MRSEC/MRL Shared Experimental Facilities at MIT, supported by the National Science Foundation under award number DMR-1419807. This work was performed in part at the Center for Nanoscale Systems (CNS), a member of the National Nanotechnology Coordinated Infrastructure Network (NNCI), which was supported by the National Science Foundation under NSF award no. 1541959. TD and JLMR also thank the Swiss National Science Foundation for grant support under PSSGI0_155986. TD would also

like to thank Dr dino Klotz for helpful discussions and analysis of the electrochemical imepdance data.

References

1. Brett, D. J. L., Atkinson, A., Brandon, N. P. & Skinner, S. J. *Chem. Soc. Rev.* **37,** 1568–1578 (2008).

2. Iftekhar Jaim, H. M., Lee, S., Zhang, X. & Takeuchi, I. *Appl. Phys. Lett.* **111,** (2017).

3. Shi, Y., Garbayo, I., Muralt, P. & Rupp, J. L. M. *J. Mater. Chem. A* **5,** 3900–3908 (2017).

4. Whittingham, M. S. *Chem. Rev.* **104,** 4271–4301 (2004).

5. Tarascon, J. M. & Armand, M. *Nature* **414,** 359–367 (2001).

6. Hu, Y.-S. *Nat. Energy* **1,** (2016).

7. Garbayo, I., Struzik, M., Bowman, W. J., Pfenninger, R., Stilp, E. & Rupp, J. L. M. *Adv. Energy Mater.* **8,** 1–14 (2018).

8. Pfenninger, R., Struzik, M., Garbayo, I., Stilp, E. & Rupp, J. L. M. *Nat. Energy* **4,** (2019).

9. Pagani, F., Stilp, E., Pfenninger, R., Reyes, E. C., Remhof, A., Balogh-Michels, Z., Neels, A., Sastre-Pellicer, J., Stiefel, M., Döbeli, M., Rossell, M. D., Erni, R., Rupp, J. L. M. & Battaglia, C. *ACS Appl. Mater. Interfaces* **10,** 44494–44500 (2018).

10. Pfenninger, R., Afyon, S., Garbayo, I., Struzik, M. & Rupp, J. L. M. *Adv. Funct. Mater.* **28,** 1800879 (2018).

11. Kim, K. J., Balaish, M., Wadaguchi, M., Kong, L. & Rupp, J. L. M. *Adv. Energy Mater.* 2002689 (2020).

12. Zhu, Y., Gonzalez-Rosillo, J. C., Balaish, M., Hood, Z. D., Kim, K. J. & Rupp, J. L. M. *Nat. Rev. Mater.* (2020).

13. Takamura, H., Okumura, K., Koshino, Y., Kamegawa, A. & Okada, M. *J. Electroceramics* **13,** 613–618 (2004).

14. Tuller, H. L. *Mater. Renew. Sustain. Energy* **6,** 1–16 (2017).

15. Muhich, C. L., Blaser, S., Hoes, M. C. & Steinfeld, A. *Int. J. Hydrogen Energy* **43,** 18814–18831 (2018).

16. Chueh, W. C. & Haile, S. M. *Philos. Trans. R. Soc. A Math. Phys. Eng. Sci.* **368,** 3269–3294 (2010).

17. Di Natale, C., Paolesse, R., Martinelli, E. & Capuano, R. *Anal. Chim. Acta* **824,** 1–17 (2014).

18. Liu, Y., Parisi, J., Sun, X. & Lei, Y. *J. Mater. Chem. A* **2,** 9919–9943 (2014).

19. Struzik, M., Garbayo, I., Pfenninger, R. & Rupp, J. L. M. *Adv. Mater.* **30,** 1–10 (2018).

20. Suzuki, K., Okamoto, T., Kondo, H., Tanaka, N. & Ando, A. *J. Appl. Phys.* **113,** (2013).

21. Wojtyniak, M., Szot, K., Wrzalik, R., Rodenbücher, C., Roth, G. & Waser, R. *J. Appl. Phys.* **113,** (2013).

22. Waser, R., Baiatu, T. & Härdtl, K. H. *Mater. Sci. Eng. A* **109,** 171–182 (1989).

23. Hennen, T., Waser, R., Menzel, S., Rupp, J. A. J. & Wouters, D. J. *Faraday Discuss.* (2018).

24. Marchewka, A., Roesgen, B., Skaja, K., Du, H., Jia, C.-L., Mayer, J., Rana, V., Waser, R. & Menzel, S. *Adv. Electron. Mater.* **2,** 1500233 (2016).

25. Menzel, S., Von Witzleben, M., Havel, V. & Böttger, U. *Faraday Discuss.* **213,** 197–213 (2019).

26. Schmitt, R., Spring, J., Korobko, R. & Rupp, J. L. M. M. *ACS Nano* **11,** 8881–8891 (2017).

27. Schweiger, S., Kubicek, M., Messerschmitt, F., Murer, C. & Rupp, J. L. M. *ACS Nano* **8,** 5032–5048 (2014).

28. Schmitt, R., Kubicek, M., Sediva, E., Trassin, M., Weber, M. C., Rossi, A., Hutter, H., Kreisel, J., Fiebig, M. & Rupp, J. L. M. *Adv. Funct. Mater.* 1804782 (2018).

29. Gonzalez-Rosillo, J. C., Balaish, M., Hood, Z., Nadkarni, N., Fraggedakis, D., Kim, K., Mullin, K. M., Pfenninger, R., Bazant, M. Z. & Rupp, J. L. . *Adv. Mater.* 1907465 (2020).

30. Lee, J. & Lu, W. D. *Adv. Mater.* **30,** 1–33 (2018).

31. Bauer, U., Yao, L., Emori, S., Tuller, H. L., Dijken, S. van & Beach, G. S. D. *Nat. Mater.* **14,** 174–181 (2014).

32. Tan, A. J., Huang, M., Avci, C. O., Büttner, F., Mann, M., Hu, W., Mazzoli, C., Wilkins, S., Tuller, H. L. & Beach, G. S. D. *Nat. Mater.* (2018).

33. Viernstein, A., Kubicek, M., Morgenbesser, M., Walch, G., Brunauer, G. C. & Fleig, J. *Adv. Funct. Mater.* **29,** (2019).

34. Huang, M., Jun Tan, A., Büttner, F., Liu, H., Ruan, Q., Hu, W., Mazzoli, C., Wilkins, S., Duan, C., Yang, J. K. W. & Beach, G. S. D. *Nat. Commun.* **10,** 1–8 (2019).

35. Emboras, A., Niegemann, J., Ma, P., Haffner, C., Pedersen, A., Luisier, M., Hafner, C., Schimmel, T. & Leuthold, J. *Nano Lett.* **16,** 709–714 (2015).

36. Koch, U., Hoessbacher, C., Emboras, A. & Leuthold, J. *J. Electroceramics* **39,** 1–12 (2017).

37. Lee, J. H., Yoon, C., Lee, S., Kim, Y. H. & Park, B. H. *ACS Appl. Mater. Interfaces* **8,** 35464–35471 (2016).

38. Chanthbouala, A., Garcia, V., Cherifi, R. O., Bouzehouane, K., Fusil, S., Moya, X., Xavier, S., Yamada, H., Deranlot, C., Mathur, N. D., Bibes, M., Barthélémy, A. & Grollier, J. *Nat. Mater.* 861–86 (2012).

39. Kim, D. J., Lu, H., Ryu, S., Bark, C.-W., Eom, C.-B., Tsymbal, E. Y. & Gruverman, A. *Nano Lett.* **12,** 5697–5702 (2012).

40. Ebong, I. E. & Mazumder, P. *Proc. IEEE* **100,** 2050–2060 (2012).

41. Joshua Yang, J., Strukov, D. B., Stewart, D. R., Yang, J. J., Strukov, D. B., Stewart, D. R., Joshua Yang, J., Strukov, D. B. & Stewart, D. R. *Nat. Nanotechnol.* **8,** 13–24 (2013).

42. Yin, X.-B., Yang, R., Xue, K.-H., Tan, Z., Zhang, X.-D., Miao, X. & Guo, X. *Phys. Chem. Chem. Phys.* (2016).

43. Lübben, M., Cüppers, F., Mohr, J., Witzleben, M. Von, Breuer, U., Waser, R., Neumann, C. & Valov, I. (2020).

44. Wang, S., Wu, L., Gao, J., He, Q. & Liu, M. *J. Power Sources* **185,** 917–921 (2008).

45. Ishihara, T., Akbay, T., Furutani, H. & Takita, Y. *Solid State Ionics* **113–115,** 585–591 (1998).

46. Huggins, R. A. *Ionics (Kiel).* **8,** 300–313 (2002).

47. Lim, D. K., Guk, J. G., Choi, H. S. & Song, S. J. *J. Korean Ceram. Soc.* **52,** 299–303 (2015).

48. Riess, I. *Solid State Ionics* **91,** 221–232 (1996).

49. Guo, X. & Maier, J. *Solid State Ionics* **130,** 267–280 (2000).

50. Kamp, B., Merkle, R. & Maier, J. *Sensors Actuators, B Chem.* **77,** 534–542 (2001).

51. Chen, D., Groß, A., Bono, D. C., Kita, J., Moos, R. & Tuller, H. L. *Solid State Ionics* **262,** 914–917 (2014).

52. Messerschmitt, F., Kubicek, M., Schweiger, S. & Rupp, J. L. M. *Adv. Funct. Mater.* **24,** 7448–7460 (2014).

53. De Souza, R. A., Martin, M., Lee, C.-E., Borchardt, G., Damjanovic, T., Borchardt, G., Ivers-Tiffée, E., Piskunov, S. & Maier, J. *Phys. Chem. Chem. Phys.* **10,** 2356 (2008).

54. Genreith-Schriever, A. R., Hebbeker, P., Hinterberg, J., Zacherle, T. & De Souza, R. A. *J. Phys. Chem. C* **119,** 28269–28275 (2015).

55. De Souza, R. A. *J. Mater. Chem. A* **5,** 20334–20350 (2017).

56. Harrington, G. F., Sun, L., Yildiz, B., Sasaki, K., Perry, N. H. & Tuller, H. L. *Acta Mater.* **166,** 447–458 (2019).

57. Mehonic, A., Shluger, A. L., Gao, D., Valov, I., Miranda, E., Ielmini, D., Bricalli, A., Ambrosi, E., Li, C., Yang, J. J., Xia, Q. & Kenyon, A. J. *Adv. Mater.* **30,** 1–21 (2018).

58. Gale, E. *Semicond. Sci. Technol.* **29,** 1–29 (2014).

59. Li, Y., Wang, Z., Midya, R. M., Xia, Q. & Yang, J. J. *J. Phys. D. Appl. Phys.* (2018).

60. Pan, F., Gao, S., Chen, C., Song, C. & Zeng, F. *Mater. Sci. Eng. R Reports* **83,** 1–59 (2014).

61. Koettgen, J., Grieshammer, S., Hein, P., Grope, B. O. H., Nakayama, M. & Martin, M. *Phys. Chem. Chem. Phys.* **20,** 14291–14321 (2018).

62. Grieshammer, S., Nakayama, M. & Martin, M. *Phys. Chem. Chem. Phys.* **3804,** 3804–3811 (2016).

63. Kalaev, D., Tuller, H. L. H. L. & Riess, I. *Solid State Ionics* **319,** 291–295 (2018).

64. Bishop, S. R., Stefanik, T. S. & Tuller, H. L. *Phys. Chem. Chem. Phys.* **13,** 10165 (2011).

65. Bishop, S. R., Stefanik, T. S. & Tuller, H. L. *J. Mater. Res.* **27,** 2009–2016 (2012).

66. Skinner, S. J. & Kilner, J. A. *Mater. Today* **6,** 30–37 (2003).

67. Kim, J. J., Bishop, S. R., Thompson, N. J., Chen, D. & Tuller, H. L. *Chem. Mater.* **26,** 1374–1379 (2014).

68. Kim, J. J., Bishop, S. R., Chen, D. & Tuller, H. L. *Chem. Mater.* **29,** 1999–2007 (2017).

69. Kalaev, D. & Riess, I. *Solid State Ionics* **241,** (2013).

70. Kalaev, D., Rothschild, A. & Riess, I. *RSC Adv.* **7,** 38059–38068 (2017).

71. Tuller, H. L. & Nowick, A. S. *J. Phys. Chem. Solids* **38,** 859–867 (1977).

72. Waldow, S. P. & De Souza, R. A. *J. Phys. Energy* **2,** 024001 (2020).

73. De Souza, R. A. *Adv. Funct. Mater.* **25,** 6326–6342 (2015).

74. Kim, J. J., Bishop, S. R., Thompson, N. ., Kuru, Y. & Tuller, H. L. *Solid State Ionics* **225,** 198–200 (2012).

75. Spiridigliozzi, L., Dell'Agli, G., Marocco, A., Accardo, G., Pansini, M., Yoon, S. P., Ham, H. C. & Frattini, D. *J. Ind. Eng. Chem.* (2018).

76. Nicollet, C., Kalaev, D. & Tuller, H. L. *Solid State Ionics* **331,** 96–101 (2019).

77. Schmitt, R., Nenning, A., Kraynis, O., Korobko, R., Frenkel, A. I., Lubomirsky, I., Haile, S. M. & Rupp, J. L. M. *Chem. Soc. Rev.* **49,** 554--592 (2020).

78. Westermann, A., Geantet, C., Vernoux, P. & Loridant, S. *J. Raman Spectrosc.* **47,** 1276–1279 (2016).

79. Kalaev, D., Defferriere, T., Nicollet, C., Kadosh, T. & Tuller, H. L. *Adv. Funct. Mater.* **30,** 1907402 (2020).

80. Lai, W. & Haile, S. M. *J. Am. Ceram. Soc.* **88,** 2979–2997 (2005).

81. Kilner, J. A. *Solid State Ionics* **129,** 13–23 (2000).

82. Nguyen, T. L., Dokiya, M., Wang, S., Tagawa, H. & Hashimoto, T. *Solid State Ionics* **130,** 229–241 (2000).

83. Zhang, T. S., Ma, J., Kong, L. B., Chan, S. H. & Kilner, J. A. *Solid State Ionics* **170,** 209–217 (2004).

84. Dyre, J. C. *J. Phys. C Solid State Phys.* **21,** 2431–2434 (1988).

85. Dalvi, A., Parvathala Reddy, N. & Agarwal, S. C. *Solid State Commun.* **152,** 612–615 (2012).

86. Metselaar, R. & Oversluizen, G. *J. Solid State Chem.* **55,** 320–326 (1984).

87. Haering, C., Roosen, A. & Schichl, H. *Solid State Ionics* **176,** 253–259 (2005).

88. Haering, C., Roosen, A., Schichl, H. & Schnöller, M. *Solid State Ionics* **176,** 261–268 (2005).

89. Robert, L. E. J. in *Essays Struct. Chem.* 291–293 (1995).

90. Gibson, I. R. & Irvine, J. T. S. *J. Mater. Chem.* **6,** 895–898 (1996).

91. Ye, F., Mori, T., Ou, D. R., Zou, J. & Drennan, J. *2005 4th Int. Symp. Environ. Conscious Des. Inverse Manuf.* 894–897 (2005).

92. Wang, D. Y., Park, D. S., Griffith, J. & Nowick, A. S. *Solid State Ionics* **2,** 95–105 (1981).

93. Chen, P. -L & Chen, I. -W. *J. Am. Ceram. Soc.* **77,** 2289–2297 (1994).

94. Rockenhäuser, C., Butz, B., Schichtel, N., Janek, J., Oberacker, R., Hoffmann, M. J. & Gerthsen, D. *J. Eur. Ceram. Soc.* **34,** 1235–1242 (2014).

95. Kabir, A., Zhang, H. & Esposito, V. in *Cerium Oxide Synth. Prop. Appl.* (2020).

96. Manning, P. S., Sirman, J. D., De Souza, R. A. & Kilner, J. A. *Solid State Ionics* **100,** 1–10 (1997).

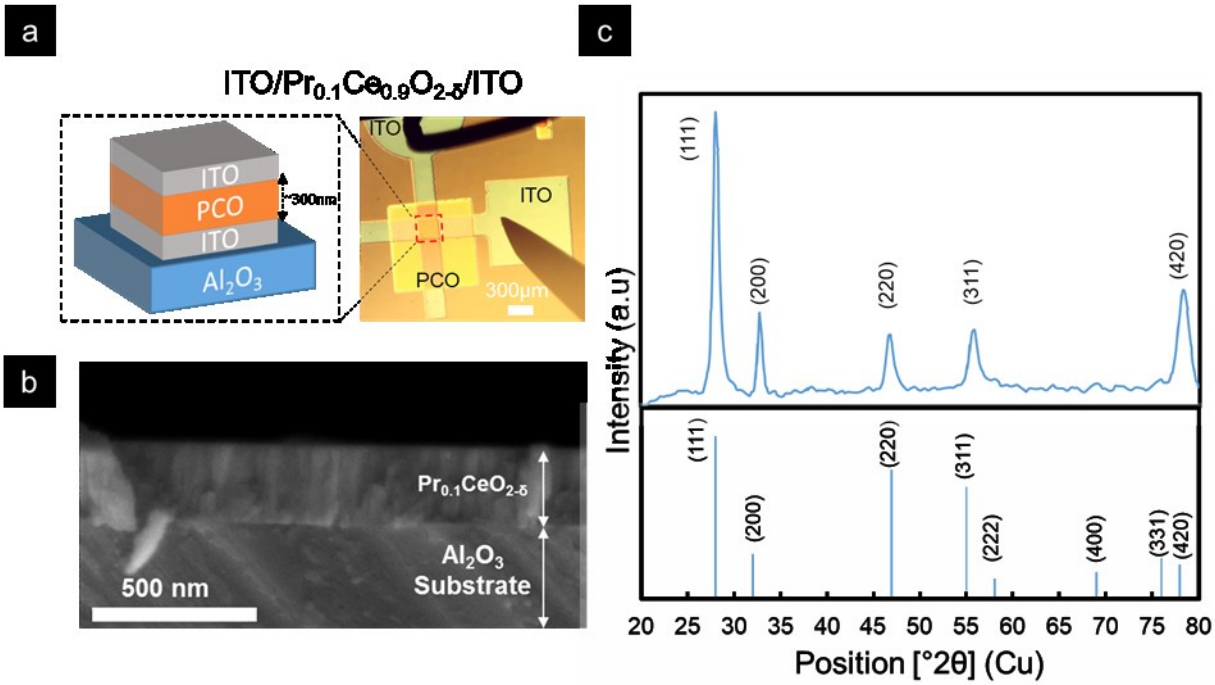

Figure 1 a) Schematic of a cross-sectional device structure and a top view optical micrograph of the prepared device. b) SEM cross-sectional image of an as-prepared $Pr_{0.1}Ce_{0.9}O_{2-\delta}$ thin film grown by pulsed laser deposition. c) Grazing incident XRD pattern of a similarly grown PLD film. By comparison with a reference $Pr_{0.1}Ce_{0.9}O_{2-\delta}$ pattern, we find that the film is polycrystalline.

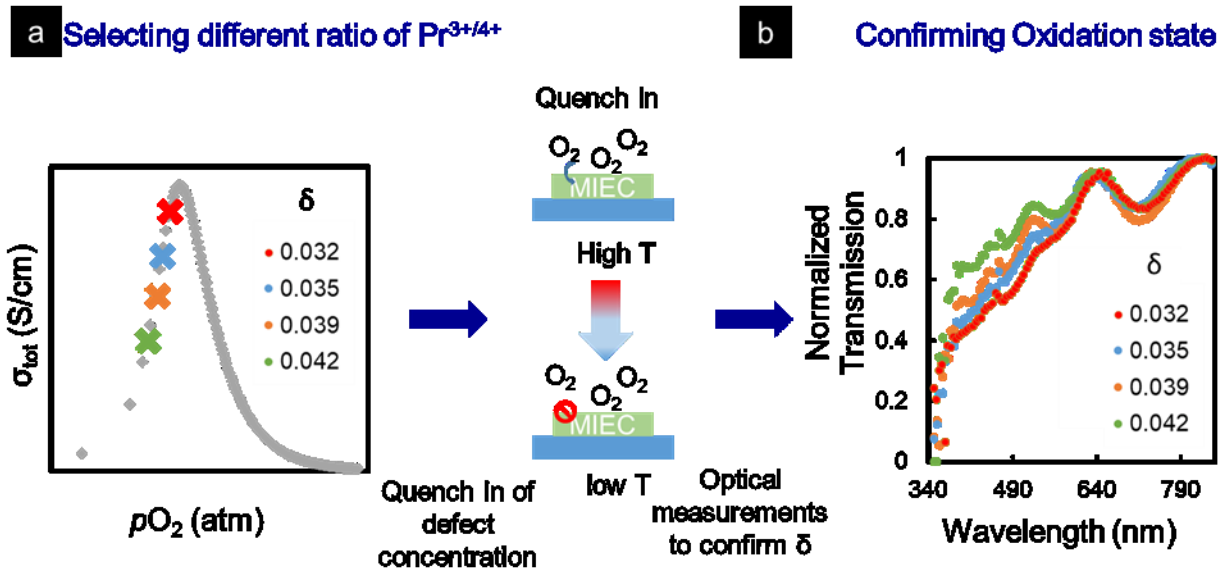

Figure 2 a) Schematic representation of the quench-in procedure, depicting the expected different regions of the σ_{tot} vs $\log_{10}(pO_2)$ curve at 50 °C for the different quenched in stoichiometries. The sample was held at an intermediate temperature (400-600 °C) while the oxygen partial pressure was modified. After several hours, but before equilibrium with pO_2 was reached, the sample was quenched to freeze in the new defect concentration. b)Transmission spectra of the device measured after quenching to room temperature from the different annealing steps.

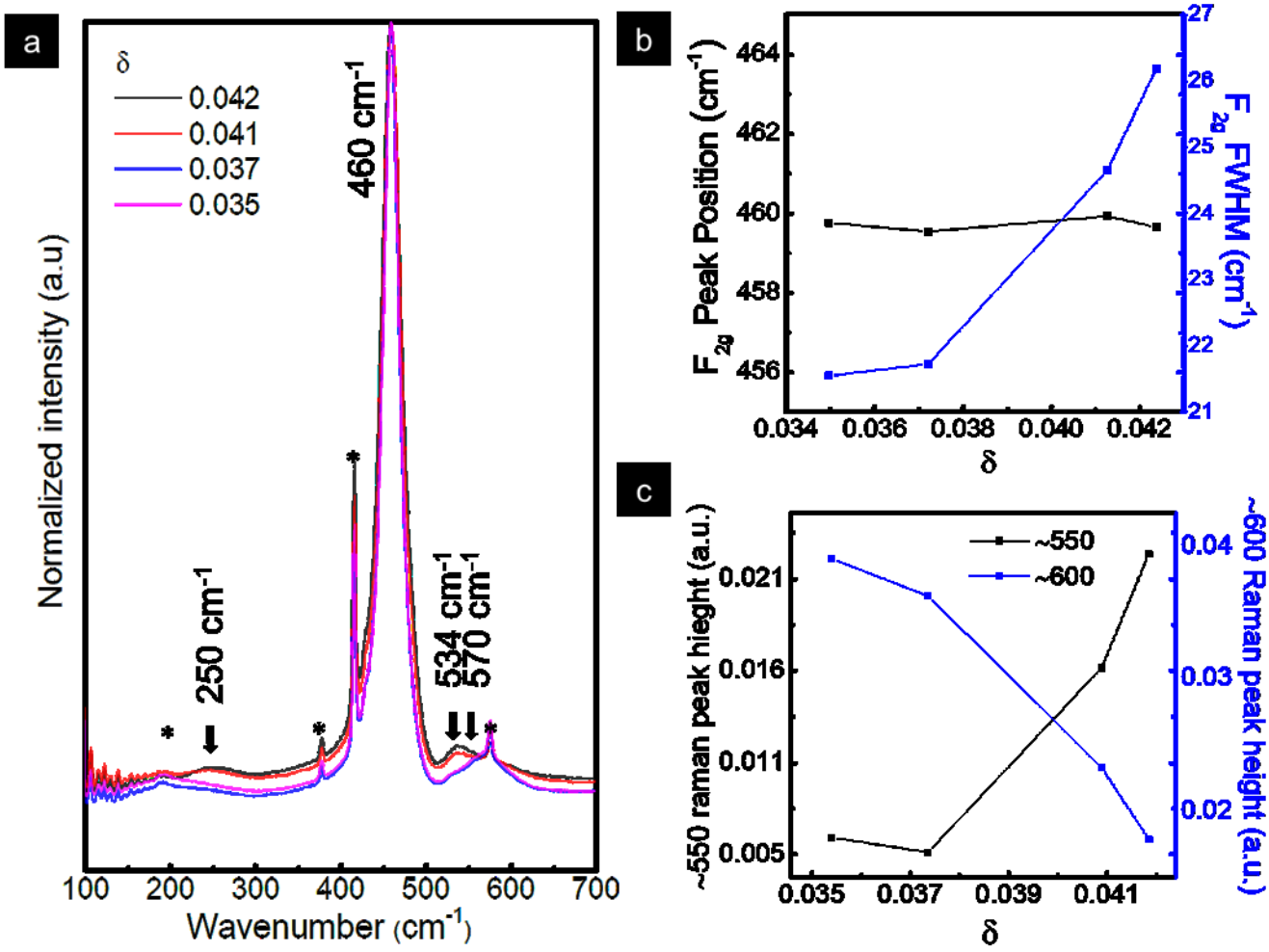

Figure 3 a) Raman spectra of the $Pr0_{.1}Ce_{0.9}O_{2-\delta}$ devices with δ varying from 0.035±0.001 to 0.042±0.001. Bands at 460 cm^{-1} denote the F_{2g} vibrational symmetry, whereas ~250cm^{-1}, ~534cm^{-1}, and ~570cm^{-1} denote oxygen vacancy activated bands. * represents ITO peaks that were disregarded from the analysis. b) Peak position (left y-axis) and FWHM (right y-axis) of the 460 cm^{-1} Raman active vibrational mode with F_{2g} symmetry for the Pr doped ceria samples for different δ; the lines serve as a guide to the eye. (c) Peak intensity of the

oxygen vacancy induced Raman vibrations denoted as ~550cm^{-1} (left y-axis) and ~600cm^{-1} (right y-axis); the lines serve as a guide to the eye.

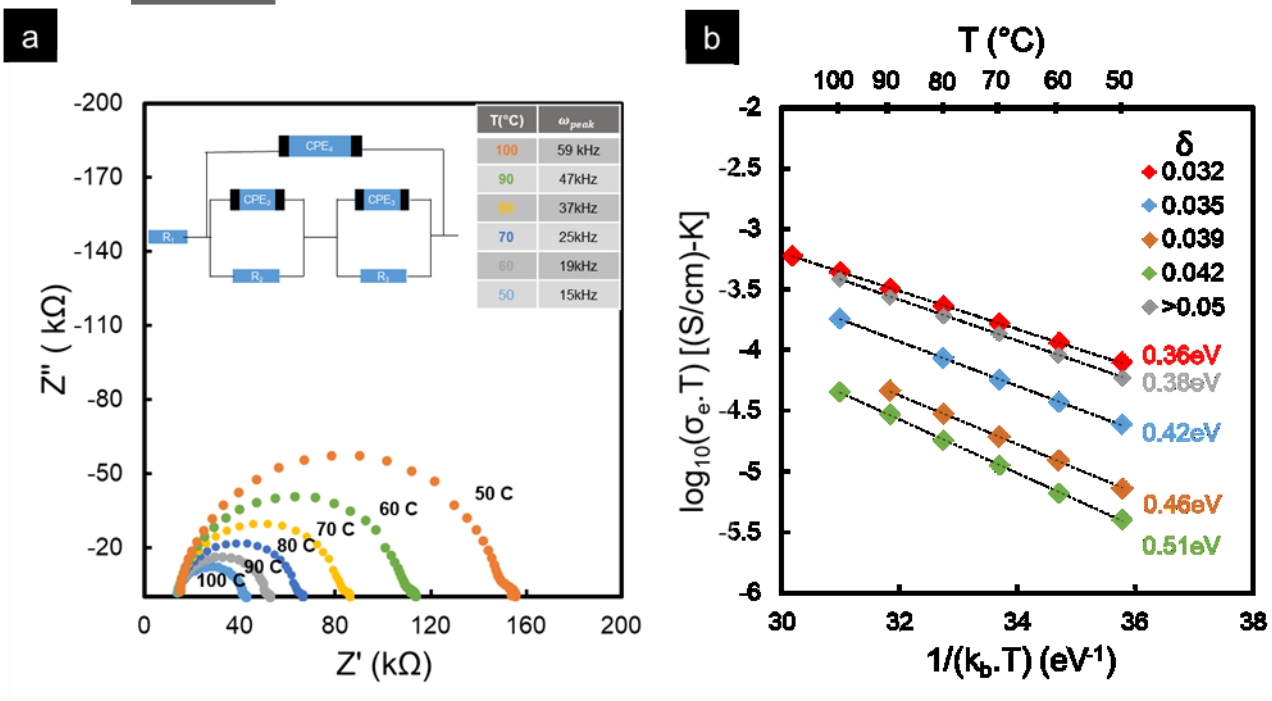

Figure 4 a) Examples of impedance spectra measurements made on the ITO/PCO/ITO (δ~0.032±0.001) device from 50 to 100°C prior to the dynamic I-V measurements. An equivalent circuit is depicted in which R1 represents the series resistance of the electrodes given by the offset resistance of the semicircle from the origin, R2 and CPE2 represent the bulk PCO equivalent circuit given by a resistance and constant phase element in parallel as reflected in the main semicircle, and R3 and CPE3 represent a similar circuit representing the interfacial electrode contributions as reflected in the small partial semicircle originating near the low-frequency intercept of the major semicircle. b) Arrhenius plot of the bulk

contribution to the total largely electronic conductivity $\sigma_{bulk} \sim \sigma_e$, for the different non-stoichiometric states of the device.

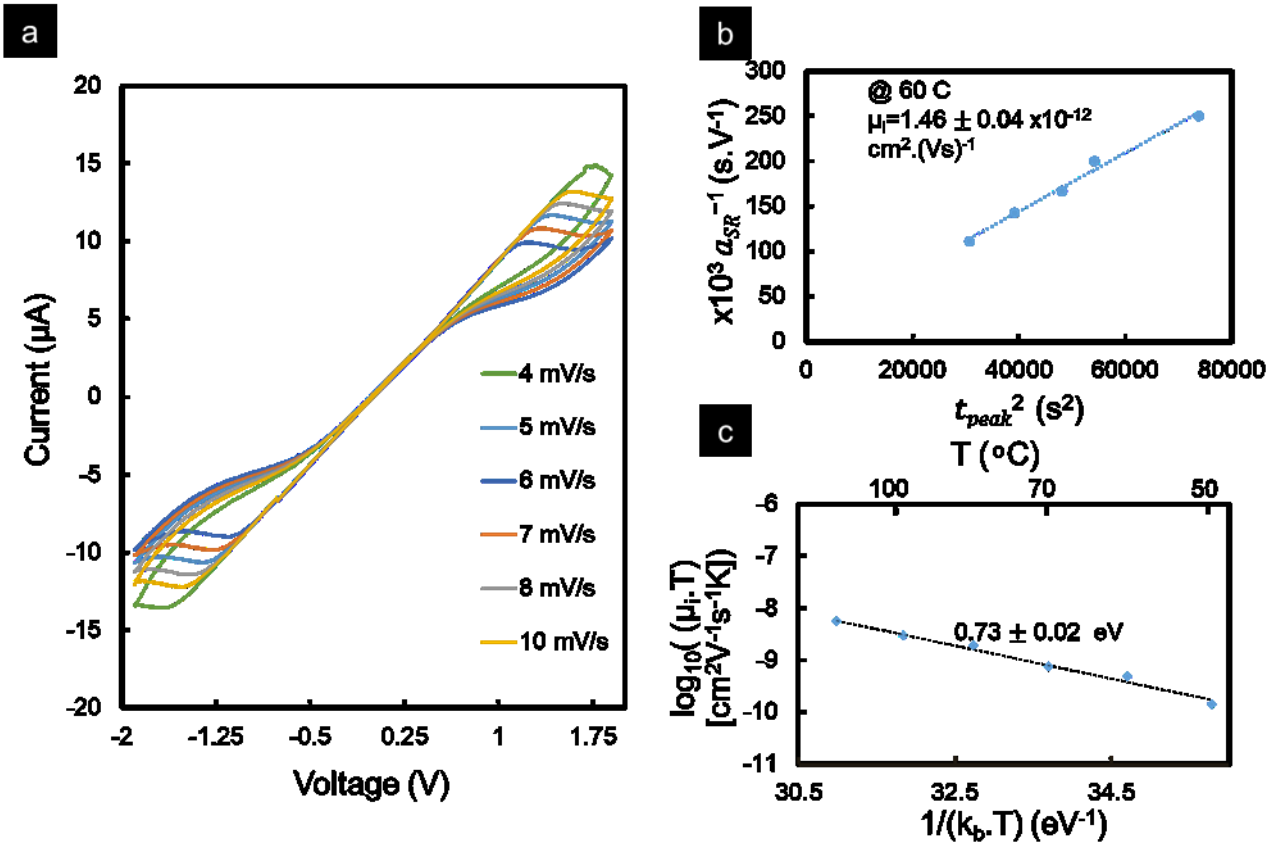

Figure 5 a) Example of the dynamic non-linear I-V response of a PCO crossbar, for sample δ~0.032±0.001, measured at 60 °C as a function of applied voltage sweep rate corrected for the electrode contribution. b) Plot of reciprocal sweep rate, versus time-current-peak squared. The dependency is observed to be linear as predicted by equation (1) corresponding to an ionic mobility, $1.46 \pm 0.04 \times 10^{-12}$ $cm^2V^{-1}s^{-1}$. c) Arrhenius plot of $\log_{10}(\mu i.T)$ vs $1/(k_b.T)$ for sample $\delta \sim 0.032 \pm 0.001$. The migration enthalpy for the oxygen vacancy mobility equals

0.73 ± 0.04 eV over the temperature range from 50-100 °C, while the y-axis intercept is 41.5 ± 0.1 $cm^2V^{-1}s^{-1}$.

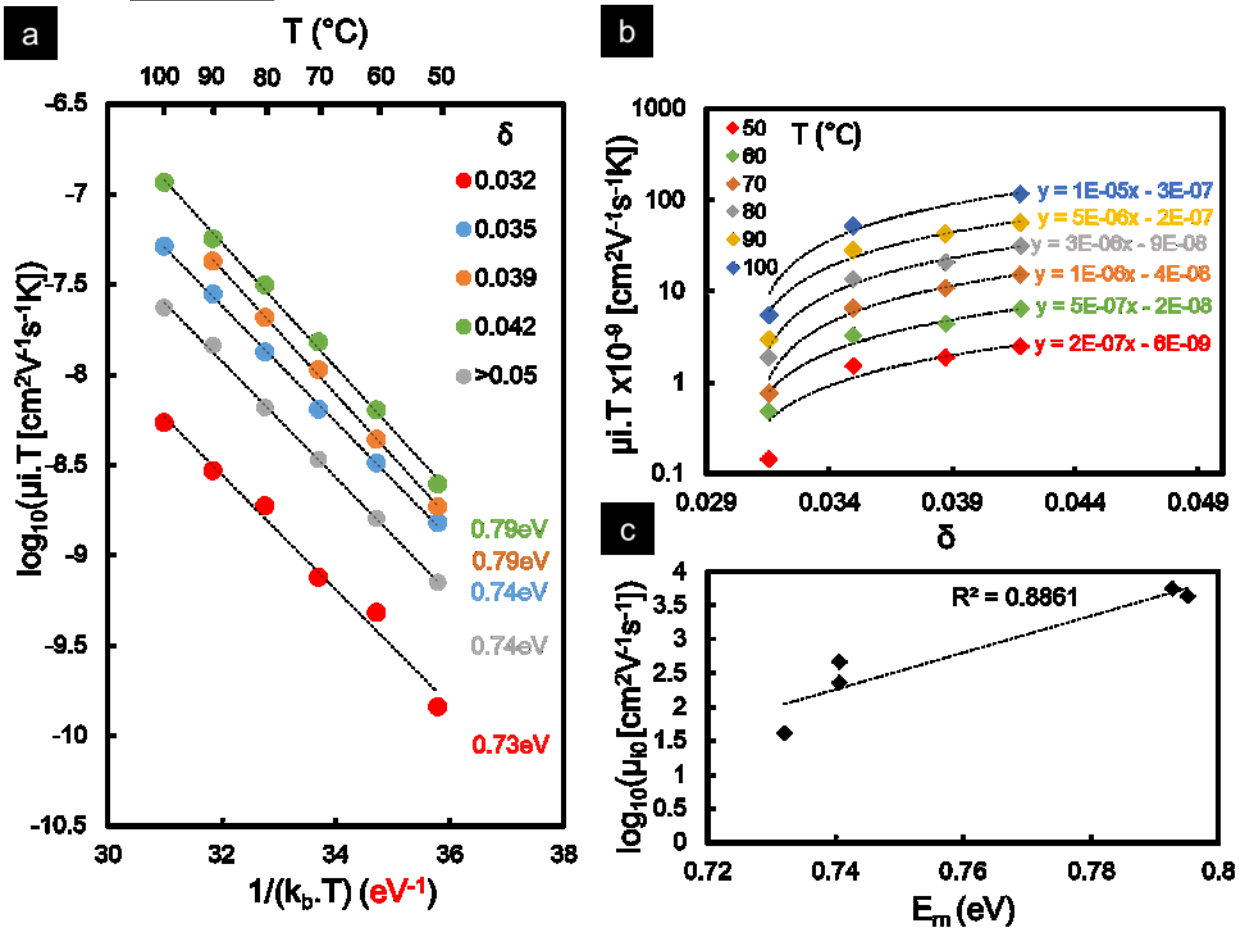

Figure 6 a) Arrhenius plot of $\log_{10}(\mu iT)$ vs $1/(k_bT)$ for the film with the different quenched in stoichiometries. The as-prepared sample (δ~0.039±0.001) exhibited a migration enthalpy of 0.79 ± 0.02 eV. Reduction of the film (δ~0.042±0.001) leads to a similar energy of 0.79 ± 0.02 eV, while oxidation (δ ~ 0.035±0.001 and 0.032±0.001) led to smaller activation energies of 0.74 ± 0.01 eV and 0.73 ± 0.04 eV, respectively. b) Semi-Log plot of $\mu_i.T$ as a function of δ for temperatures from 50-100 °C. At each temperature, the product $\mu_i.T$ is fitted

with a linear curve on concentration with slopes varying from 2.15 ± 0.4 x 10^{-7} to 1.07 ± x 0.1 10^{-5}, while the intercept shows an increase from -6.38±1.6 x10^{-9} $cm^2V^{-1}s^{-1}$ to -3.31±0.36 x10^{-7} $cm^2V^{-1}s^{-1}$. In semi-Log plot, the linear fit looks logarithmic. c) Plot of $\log_{10}(\mu_{i,0})$ vs E_m for the different samples measured, showing a positive linear correlation.

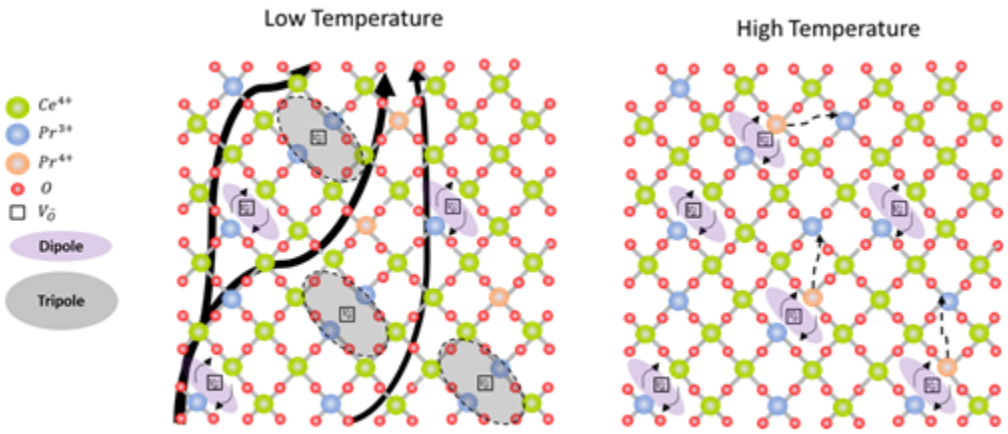

Figure 7 Schematic representation of the ordering process at constant non-stoichiometry. On the left represent a low temperature anneal case where small polarons are ordered with oxygen vacancies to form tripoles and dipoles. The migration pathway is constricted by the tripoles. On the right is high temperature anneal case where disorder is recovered by breaking up the tripoles due to the mobile small polaron.

By combined use of systematic annealing and optical monitoring, we demonstrated a 13 fold change in near room temperature oxygen vacancy ionic mobility in $Pr_{0.1}Ce_{0.9}O_{2-\delta}$ thin films, highlighting the sensitivity of ionic transport to processing induced ordering in a model polaronic mixed conductor. Such insights are crucial for understanding the potential origins of variations in ionic transport in nanoionic devices.